Atmospheric Analysis of the M/L– and M/T–Dwarf Binary Systems LHS 102 and Gliese 229

S.K. Leggett,[1] Peter H. Hauschildt,[2] F. Allard,[3] T.R. Geballe,[4] E. Baron,[5]

[1] *Joint Astronomy Centre, University Park, Hilo, HI 96720, Email:* `skl@jach.hawaii.edu`

[2] *Dept. of Physics and Astronomy & Center for Simulational Physics, University of Georgia, Athens, GA 30602-2451; Email:* `yeti@hal.physast`

[3] *CRAL, Ecole Normale Superieure, 46 Allee d'Italie, Lyon, 69364 France; Email:* `fallard@cral.ens-lyon.fr`

[4] *Gemini Observatory, University Park, Hilo, HI 96720; Email:* `tgeballe@gemini.edu`

[5] *Dept. of Physics and Astronomy, University of Oklahoma, 440 W. Brooks, Rm 131, Norman, OK 73019-0260; Email:* `baron@nhn.ou.edu`

1 February 2008

ABSTRACT

We present 0.9—2.5μm spectroscopy with R$\sim$800 and 1.12-1.22μm spectroscopy with R$\sim$5800 for the M dwarfs Gl 229A and LHS 102A, and for the L dwarf LHS 102B. We also report $IZJHKL'$ photometry for both components of the LHS 102 system, and L' photometry for Gl 229A. The data are combined with previously published spectroscopy and photometry to produce flux distributions for each component of the kinematically old disk M/L–dwarf binary system LHS 102 and the kinematically young disk M/T–dwarf binary system Gliese 229. The data are analyzed using synthetic spectra generated by the latest "AMES-dusty" and "AMES-cond" models by Allard & Hauschildt. Although the models are not able to reproduce the overall slope of the infrared flux distribution of the L dwarf, most likely due to the treatment of dust in the photosphere, the data for the M dwarfs and the T dwarf are well matched. We find that the Gl 229 system is metal–poor despite having kinematics of the young disk, and that the LHS 102 system has solar metallicity. The observed luminosities and derived temperatures and gravities are consistent with evolutionary model predictions if the Gl 229 system is very young (age ~ 30 Myr) with masses (A,B) of $(0.38, \gtrsim 0.007)M_\odot$, and the LHS 102 system is older, aged 1—10 Gyr with masses (A,B) of $(0.19, 0.07)M_\odot$.

1   INTRODUCTION

In the last few years there have been dramatic developments in the study of very low mass stars and brown dwarfs — where the latter are defined to be objects with mass below that required for stable hydrogen burning. Sky surveys have found a significant population of low mass dwarfs cooler than M–dwarfs. The first population to be identified was the L–dwarf class, distinguished from the M–dwarfs by weakening VO and TiO absorption features in the red, and by stronger alkaline and H_2O absorption features in the red and near–infrared (e.g. Delfosse et al. 1987; Kirkpatrick et al. 1999; Martín et al. 1999). The L–dwarfs cover an effective temperature range of about 2200 K to 1400 K (e.g. Leggett et al. 2002) and the prototype of this class is GD 165B, discovered by Becklin & Zuckerman (1988) as a red companion to a hot white dwarf. Several objects even cooler than the L–dwarfs were discovered in 1999 by the Sloan Digital Sky Survey and the 2 Micron All–Sky Survey (Strauss et al. 1999; Burgasser et al. 1999). They are very similar to Gliese 229B, the extremely low–mass companion to an M–dwarf found by Nakajima et al. (1995), and are distinguished by the presence of CH_4 absorption in the near–infrared H and K bands. These objects, known as T–dwarfs, have $T_{\rm eff}$ ∼1300—800 K and tens of T–dwarfs are now known (see Geballe et al. 2002; Burgasser et al. 2002, and references therein).

In this paper we present an analysis of the low–mass binary systems LHS 102 and Gliese (Gl) 229. The primaries of these two systems are M–dwarfs which are in the proper motion catalogues by Luyten (1979) and Gliese & Jahreiss (1991). The secondaries were only recently detected. Gl 229B, the prototypical T–dwarf, was discussed above; LHS 102B is an L dwarf discovered by Goldman et al. (1999). We present new UKIRT infrared photometry and spectroscopy of these objects in §2, which are analyzed using the latest models by Allard & Hauschildt (Hauschildt, Allard & Baron 1999), described in §3. The results of the model comparison are given in §4, the implications for age and mass of each component are discussed in §5 and our conclusions given in §6. These two systems span the newly defined low–mass spectral classes and, being binaries at known distances where each component has presumably the same chemical composition and age, are potentially very useful for constraining atmospheric and evolutionary models of ultracool dwarfs.

2   OBSERVATIONAL RESULTS

2.1 The Sample

Table 1 gives the LHS and Gliese or Gliese–Jahreiss catalogue numbers (Luyten 1979; Gliese & Jahreiss 1991) for the two systems discussed in this work. Although both primaries are in both catalogues we follow tradition and refer to one as LHS 102 and the other as Gl 229. The coordinates in the Table are based on our observations at UKIRT and are accurate to about an arcsecond.

Spectral types also are listed in Table 1. For the M dwarfs LHS 102A and Gl 229A these have been taken from Martín et al. (1999) and Leggett (1992), respectively. The T subtype for Gl 229B is taken from the provisional classification scheme of Geballe et al. (2002). For LHS 102B the indices presented by Geballe et al. imply L4.0 based on the red spectrum, L4.0 based on the K spectrum, and a later type of L6.5 based on the H–band water index. As the last region is slightly noisier than the others we adopt a type of L4.5±0.5. This is consistent with previously published classifications based on red spectra only: Martín et al. (1999) classify this object as L4, Kirkpatrick et al. (2000) classify it L5.

Table 1 also gives the kinematic population for each system, based on the space motion of the primaries, where distances were obtained from the Hipparcos Catalogue for Gl 229 (Perryman et al. 1999) and from the Yale Catalogue for LHS 102 (van Altena et al. 1994). The population for the Gl 229 system is from Leggett (1992); we determine the population for the LHS 102 system to be older, based on the specifications given by Leggett for UVW space motions. The space motions for LHS 102A were calculated using a radial velocity from Rodgers & Eggen (1974); a more recent but quite different value for the secondary from Basri et al. (2000) gives the same end result — that the V motion at −73 (for LHS 102A) or −77km/s (for LHS 102B) is too large for the "young" disk.

2.2 New Photometry and Observed Colours

New photometry has been obtained for three of the stars in the sample. In 1999 August, $IZJHK$ was obtained for the LHS 102 system using the UK Infrared Telescope (UKIRT) with the UFTI camera, a 1024×1024 imager with $0\rlap{.}''09$ pixels. The I and Z filters are non–standard and have half–power bandwidths of 0.72—0.93 μm, and 0.85—1.055 μm. Landolt (1992) standards were used to calibrate the I data and provisional Sloan standards were used for the Z data (Krisciunas et al. 1998). For both I and Z there are strong colour terms

between the UFTI system and the Landolt and Sloan systems; the results are given in Table 2 in the natural UFTI system.

The UFTI JHK filters are part of Mauna Kea consortium filter set (Simons & Tokunaga 2002; Tokunaga & Simons 2002). UKIRT faint standards (Hawarden et al. 2001) were used to calibrate the photometry. There are colour differences between the IRCAM3 system used to establish the UKIRT faint standards and the natural UFTI system, defined by the new filter set (for more discussion see Hawarden et al. 2001; Leggett et al. 2002). In Table 2 we list JHK in the natural UFTI or Mauna Kea consortium (also known as MKO) system.

New L$'$ photometry was obtained for LHS 102 A and B, and Gl 229A, in 1999 September, using UKIRT's IRCAM/TUFTI camera, a $256{\times}256$ imager with $0\rlap{.}''08$ pixels. Bright UKIRT standards were used to calibrate the photometry. The L$'$ magnitudes of late L dwarfs and T dwarfs are different for the Mauna Kea consortium filter and the filter previously installed in IRCAM and referred to as the UKIRT filter (see Leggett et al. 2002; Stephens et al. 2001); the results in Table 2 are on the MKO system.

Table 3 gives for both systems the distances taken from the parallax catalogues (Perryman et al. 1999; van Altena et al. 1994) in the form of distance moduli, and tabulates $IZJHKL'$ colours for the sample. In this Table we give I magnitudes on the Cousins system. The value for Gl 229A is taken from the compilation by Leggett (1992). For the other three objects the I_C value is synthesized from the flux–calibrated spectral energy distributions using a filter profile from Bessell (1990) (red spectra from the literature have been added to the infrared spectra, see §2.3). For Gl 229B we extended the available spectroscopic data shortwards of 0.8μm to 0.7μm using as a template the energy distributions for the similar object in Strauss et al. (1999). The uncertainties in I for Gl 229B and LHS 102A,B are $\sim 10\%$. We suggest that these values for I are preferable to those reported by Goldman et al. (1999) for LHS 102 A and B, which are inconsistent with our flux distributions, as is the value for LHS 102A reported by Rodgers & Eggen (1974); i.e. adoption of either of these earlier results would lead to a discontinuity in the observed red to near–infrared flux distribution. The Z magnitudes for Gl 229 A and B are synthesized from their spectral energy distributions (the primary would saturate UFTI and the secondary is contaminated by the primary in imaging mode); the uncertainties are $\sim 10\%$. The MKO system JHK for Gl 229A are synthesized from our flux–calibrated spectral energy distributions (the spectra were flux calibrated using the photometry reported in Leggett 1992); the uncertainties are $\sim 5\%$.

2.3   New Spectroscopy and Spectroscopic Sequences

New R∼5800 spectroscopic data for 1.12—1.22μm for Gl 229A and LHS 102A,B were obtained during 1999 August—November, using the CGS4 spectrometer on UKIRT. Telluric features were removed by ratioing with a nearby A– or F–type star (after removing hydrogen lines present in the ratio star spectrum). The data were obtained in two spectral segments which were then joined around 1.16–1.17 μm. Data with R∼3000 over narrow intervals in the J, H and K bands for Gl 229B were taken from Saumon et al. (2000) and also used in this analysis.

Spectra at R∼800 covering 0.86—2.52 μm for Gl 229A and LHS 102A, and 0.83—2.52 μm for LHS 102B, were obtained on 1999 September and August, also using CGS4 on UKIRT. Telluric features were removed by ratioing with nearby A– or F–type stars (after removing hydrogen lines present in the ratio star spectrum). The spectra consisted of several segments, each segment was flux calibrated using our photometry and conjoined with adjacent segments to form spectral energy distributions. We excluded the range 1.36—1.41 μm where terrestrial H_2O absorption makes the data too noisy to be useful.

The 0.84—4.15 μm spectra for Gl 229B is taken from Leggett et al. (1999) who re–flux–calibrated the red and L–band spectra of Oppenheimer et al. (1998) and the near–infrared spectra of Geballe et al. (1996) using photometry. These data have been further refined by putting the Oppenheimer et al. data onto vacuum wavelengths and calibrating them using the HST photometry of Golimowski et al. (1998). We also use the R∼480 4.5—5.1 μm spectrum of Gl 229B from Noll et al. (1997). This spectrum is not flux calibrated photometrically, and the flux level may be uncertain by ∼30% (due to possible differences in slit losses between Gl 229B and the calibration star).

Spectra shortwards of 0.86 μm have been taken from Henry et al. (1994) for Gl 229A (R≈400), from Henry et al. (2002) for LHS 102A (R≈700), and from Martín et al. (1999) for LHS 102B (R≈700). The blue ends of the CGS4 spectra were calibrated using our Z and J photometry and the red spectra were scaled to match the CGS4 data in the region of overlap.

2.4   Integrated Fluxes and Bolometric Corrections

Table 3 gives integrated fluxes for the sample, expressed as fluxes at the Earth, bolometric magnitudes and intrinsic stellar luminosities. The updated results for Gl 229B are expressed

on the MKO system (also presented in Leggett et al. 2002). For the remaining objects, the integrated fluxes were obtained by integrating the spectroscopic data over wavelength, and adding the flux contributions at shorter and longer wavelengths. The shorter wavelength flux contribution was adopted to be a simple linear extrapolation to zero flux at zero wavelength for LHS 102B, but for Gl 229A the B magnitude (Leggett 1992), and for LHS 102A the B and V magnitudes (Rodgers & Eggen 1974), were used to estimate the shorter wavelength flux distributions, using an effective wavelength approach. The flux contributions at wavelengths beyond 2.4μm were calculated by deriving the fluxes at L$'$ using an effective wavelength approach, including the contributions between the long wavelength end of the K–band spectrum to the L$'$ wavelength, determined by linear interpolation, and assuming Rayleigh–Jeans tails beyond L$'$. The last is a reasonable assumption for M– and mid–L– dwarfs, but not for methane dwarfs, as discussed in Leggett et al. (1999). The uncertainties are 5%, 0.05 mag and 0.02dex in total flux, bolometric correction and $\log_{10}L/L_\odot$, respectively. The luminosities are used later in our analysis, together with the derived atmospheric parameters, to constrain masses and ages for the binaries.

3   MODELS AND COMPARISON TO SYNTHETIC SPECTRA

3.1   Models

The models used for this work were calculated as described in Allard et al. (2001), and are based on the Ames H_2O and TiO line lists by Partridge & Schwenke (1997) and Schwenke (1998). We stress that large uncertainties persist in these opacities for the temperature range of this work (see Allard et al. 2000). Test calculations performed by replacing the Ames water with the water line list from the SCAN database (Jørgensen et al. 2001), for somewhat lower temperatures, show relatively small effects at low spectral resolution; therefore we retained the Ames H_2O line list for this analysis. The models and their comparisons to earlier versions are the subject of a separate publication (Allard et al. 2001) and we thus do not repeat their detailed description here.

The models have been upgraded with (i) the replacement of the JOLA (Just Overlapping Line Approximation) opacities for FeH, VO and CrH by opacity sampling line data from Phillips & Davis (1993) and R. Freedman (NASA-Ames, private communication), and (ii) the extension of our database of dust grain opacities from 10 to 40 species. In the following, these models will be referred to as "AMES-dusty" for models in which the dust particles

stay in the layers in which they have formed, and "AMES-cond" for models in which the dust particles have sunk below the atmospheric layer where they originally formed (and below the photosphere). The term "AMES grid" refers to either of the "AMES-dusty" or "AMES-cond" models.

In order to investigate the effects of mixing length on the model structure and synthetic spectra, the AMES grid was extended to include mixing lengths ℓ of 1.5 and 2.0 times the local pressure scale height H_p for the parameter range of interest. These additional models were otherwise constructed with the same setup as those discussed in Allard et al. (2001) to avoid systematic errors in the analysis.

The primaries (A components) analyzed in this paper have effective temperatures that are too high for dust to form and to affect their atmospheres. These relatively high effective temperatures allow us to compare the data with the NextGen grid of model atmospheres for dwarfs (Hauschildt, Allard & Baron 1999) and giants (Hauschildt et al. 1999) and thus to compare the results obtained using older and newer model grids. The T dwarf Gl 229B is in the regime where dust has formed and settled below the atmosphere (cf. Allard et al. 2001) whereas the L dwarf LHS 102B is in the regime where dust formation and opacities have to be considered. For each of these cooler objects we use the newer and appropriate models for the analysis (see §4.2 and §4.4).

3.2   Comparison Process

Several model atmosphere grids were generated, covering the range $500 \, \text{K} \leq T_{\text{eff}} \leq 4000 \, \text{K}$, $3.5 \leq \log(g) \leq 5.5$ and [M/H]$= -1.0, -0.7, -0.5$ and 0.0 for mixing lengths of 1.0, 1.5 and 2.0, for a total of ≈ 300 model atmospheres. Synthetic spectra generated by these models were compared to the observed spectra using an IDL program. In addition, the observed spectra were compared against the NextGen grid (Hauschildt, Allard & Baron 1999) over a wider range in metallicity but for only one value of the mixing length, in order to assess the stability of the derived parameters and to search for systematic problems.

First, the resolution of the synthetic spectra was degraded to that of each observed spectrum by convolution with a Gaussian of the appropriate width, and the spectra were normalized to unit area for scaling. Next, for each observed spectrum the program calculated a quality function q, similar to a χ^2 value, for the comparison with all synthetic spectra in the grid. The quality function is calculated by first scaling the model spectrum to the observed

fluxes, then mapping the synthetic spectrum (reduced to the resolution of the observed data) onto the grid of observed wavelength points, and, finally, calculating

$$q = \sum_i w_i \left(0.5 \frac{f_i^{\text{model}} - f_i^{\text{obs}}}{f_i^{\text{model}} + f_i^{\text{obs}}} \right)^2$$

with $w_i = 0.5(f_{i+1}^{\text{obs}} + f_i^{\text{obs}})(\lambda_{i+1}^{\text{obs}} - \lambda_i^{\text{obs}})$ where f^{model} is the (mapped) flux of the model spectrum, f^{obs} is the observed flux, and λ^{obs} the observed wavelength.

We selected the models that resulted in the 3—10 lowest q values as the most probable parameter range for each individual star. The "best" value was chosen by visual inspection. This procedure allows a rough estimate of the uncertainty in the stellar parameters. Note that it does not eliminate systematic errors in the stellar parameters due to missing, incorrect or incomplete opacity sources. Table 4 lists model parameters and the goodness of fit value for each object, for models with a range of parameters selected to cover the probable range. Only the relative value of q is important, the actual value is arbitrary as it depends on the number of data points used and on the absolute flux levels; a decreasing value indicates a better fit.

4   RESULTS

4.1   LHS 102A

The spectrum of LHS 102A together with the best fitting synthetic spectra generated from the Ames grid models is presented in Fig. 1. The best fitting models have $T_{\text{eff}} \approx 3200\,\text{K}$ and $\log(g) \approx 5.0$, with solar abundances. The formal uncertainty is about $100\,\text{K}$ in T_{eff} and 0.5 in $\log(g)$. Metal poor models gave a significantly worse fit as indicated in Table 4. NextGen model fits to LHS 102A result in derived parameters of $T_{\text{eff}} \approx 3400\,\text{K}$, $\log(g) \approx 5.5$ and solar abundances. However although the NextGen models include both metal-rich and metal-poor models, the mixing length is fixed at $\alpha = 1.0$. Considering the results from all sets of fits, we conclude that $T_{\text{eff}} \approx 3200\,\text{K}$, $\log(g) \approx 5.0$, solar abundances, and $\alpha = 2.0$ are the likely parameters for LHS 102A.

The fits to the high-resolution spectrum of LHS 102A are shown in Figs. 2 and 3. We have used the Ames grid models to generate high-resolution synthetic spectra in the parameter range $(T_{\text{eff}}, \log(g))$ found from the low-resolution fitting and selected the three models that best fit the high-resolution spectra. Many of the observed lines are reproduced quite well in the synthetic spectra, indicating that the derived parameters and their ranges are good.

There are no strong indications for non-solar patterns that can be established with confidence from the data, but spectral lines from more elements are required to confirm this result.

4.2   LHS 102B

In Fig. 4 we show the observed spectrum and best fits to LHS 102B using "AMES-dusty" models from Allard et al. (2001); for comparison we show the results obtained using "AMES-cond" models (in which the dust grains are assumed to have settled completely below the atmosphere) in Fig. 5. As to be expected, the "AMES-dusty" models result in substantially better fits to the water bands than the "AMES-cond" models, although neither reproduces the heights of both the J–band and K–band flux peaks. LHS 102B's derived atmospheric parameters are $T_{\rm eff} = 1900\,{\rm K} \pm 100\,{\rm K}$, $\log(g) \approx 6.0$, solar abundances; at this temperature dust formation and opacities are important (Allard et al. 2001). The parameters derived by the fitting procedure using "AMES-dusty" and "AMES-cond" models are quite similar. This increases our confidence in the derived set of parameters, as the "AMES-dusty" and "AMES-cond" models are extreme cases and partial settling models (under construction) will fall in between these limits (see Allard et al. 2001, for more details). The model parameters listed in Table 4 are for the "AMES-dusty" model grid.

The "AMES-dusty" fit to the high resolution spectrum of LHS 102B is shown in Fig. 6. The synthetic spectra fit the atomic line profiles quite well and many molecular bands (hundreds of overlapping line for multiple systems) are reproduced reasonably well. As in the case of LHS 102A, the spectrum is well fit with solar abundances.

4.3   Gl 229A

Fig. 7 shows the best fit to the low resolution spectrum of Gl 229A. The automatic fitting procedure yielded a best fitting model from the Ames grid with the parameters $T_{\rm eff} = 3700\,{\rm K}$, $\log(g) = 4.0$, [M/H] $= -0.5$ and a mixing length parameter $\alpha = \ell/H_p = 2.0$. However, a model with $\alpha = 1.5$ fits only marginally worse (Fig. 7) for the same effective temperature and gravity. The third best fit is significantly worse in quality than the first two and gives parameters of $T_{\rm eff} = 3600\,{\rm K}$, $\log(g) = 4.5$, [M/H] $= -0.5$ and $\alpha = 1.0$. Table 4 shows that solar metallicity models gave significantly worse fits. Repeating the fitting procedure with NextGen models gave best fits in the range of $3500\,{\rm K} \leq T_{\rm eff} \leq 3600\,{\rm K}$, $3.5 \leq \log(g) \leq 4.0$, $-1.5 \leq$ [M/H] ≤ -1.0. The mixing length of the NextGen grid is fixed at $\alpha = 1.0$ and the

quality of the NextGen fits is noticeably worse, the AMES grid models (even at $\alpha = 1.0$) fit the observed spectra much better. We conclude that Gl 229A is somewhat metal poor, $[\text{M/H}] \approx -0.5$, and that the best fitting mixing length parameter α is between 1.5 and 2.0. The latter is consistent with 3D hydrodynamical models of objects in this effective temperature regime (Ludwig et al. 2002).

The comparison of the Ames grid models to the high resolution spectra is shown in Figs. 8 and 9. Fig. 8 indicates that scaled solar metallicities may not be a good assumption for Gl 229A: the lines of Fe I are systematically too strong whereas the lines of Na I are too weak in the synthetic spectra. The K I λ1177 doublet is too weak in the models (Fig. 9), but this comparison is uncertain because just longward of the K I doublet there is some blending with Fe I lines. We note that Schiavon et al. (1997) derived $[\text{Fe/H}] = -0.2$ for Gl 229A based on the FeH band at 1μm, however Mould (1978) found $[\text{M/H}] = +0.15$ based on Fourier analysis of Al, Ca and Mg infrared lines. These conflicting results in the literature may support a non–solar metallicity pattern for this star.

4.4   Gl 229B

The best fits for Gl 229B are shown in Fig. 10. For this object all model fitting was done by hand as the strong water and methane absorption bands gave rise to erroneous results using the automated routine. The range of parameters for Gl 229B is $T_{\text{eff}} = 1000\,\text{K} \pm 100\,\text{K}$, $\log(g) \lesssim 3.5$ and $[\text{M/H}] \approx -0.5$, putting it firmly into the "AMES-cond" regime; "AMES-dusty" models cannot fit its spectrum at all. The results corroborate the fits of Gl 229A with lower metallicity models so that the Gl 229 system does indeed seem to have low metallicities despite it being a member of the kinematic young disk. Solar abundance models do in general deliver worse fits than those with $[\text{M/H}] = -0.5$ (see Fig. 10), and models with even lower metallicities did not give better fits. Other authors have also suggested that Gl 229B is metal-poor; Griffith & Yelle (2000) find $[\text{O/H}] = -0.5$ based on their model analysis of the 0.8—$1.0\,\mu$m spectrum, and Saumon et al. (2000), in an analysis of the same infrared spectra studied here, find atmospheric parameters $T_{\text{eff}} = 870 - 1030\,\text{K}$, $\log(g) = 4.5 - 5.5$ and $[\text{M/H}] = -0.5 - -0.1$. Although young metal–poor stars are uncommon they do exist, as shown by Feltzing et al. (2001), in particular their Figures 13(e) and 18(a).

The fits to high resolution spectra of Gl 229B are shown in Figs. 11–13. For the most part the synthetic spectra fit the atomic line profiles quite well, but significant discrepancies

remain, in particular in the 1.5–1.7 μm range (Fig. 12). These problems are likely caused in part by incomplete molecular line data, in particular water vapor and methane. The analysis roughly confirms the results from the low resolution spectra.

5   COMPARISON TO EVOLUTIONARY MODELS

Table 5 lists the best fit model parameters, together with the observed luminosities of each of our targets. These results can be used to constrain mass and age for each component through evolutionary models. We used recent evolutionary models but were obliged to use three different models for the comparison as each covered a limited range in temperature and mass. For the M dwarfs LHS 102A and Gl 229A we used the solar-metallicity and metal-poor models of Baraffe et al. (1998), for the L dwarf LHS 102B those by Chabrier et al. (2000), and for the T dwarf Gl 229B those by Burrows et al. (1997, 2001). The first two models use earlier generation "AMES-dusty" atmospheres, the last a "cond"–type atmosphere with the dust not contributing to the atmospheric opacity. The T dwarf comparison is based on a solar metallicity evolutionary model and is therefore more uncertain than the others. We constrain the age of Gl 229B to be that of Gl 229A, and use the evolutionary models to determine mass based on age, luminosity, temperature and gravity. These give self-consistent results, however Burrows et al. (2001) show that for a given luminosity or temperature, and fixed age, a more metal-poor brown dwarf has a higher mass than a solar metallicity brown dwarf, and so we regard the value derived here for the mass of Gl 229B to be a lower limit.

To determine the possible ranges in mass and age for each component of the two binaries, we adopted uncertainties in effective temperature of 100 K, in $\log(g)$ of 0.5 dex, and in $\log_{10} L/L_\odot$ of 0.02 dex. The metallicity was considered to be fixed as evolutionary models are only available with either [M/H] $=0$ or [M/H] $= -0.5$. Assuming that the components of each binary have the same age, we find that the Gl 229 system is very young (aged 16—45 Myr) with masses for (A,B) of $(0.30—0.45, \gtrsim 0.007)M_\odot$, and the LHS 102 system is older, aged 1—10 Gyr with masses $(0.19, 0.07)$M$_\odot$. The ages are consistent with the kinematically implied disk populations (Table 1), although Nakajima et al. (1995) suggests that the lack of Hα emission in Gl 229A implies an age older than 100 Myr. We note however that the star is a flare star, which supports a young age. The young age of the Gl 229 system gives rise to a lower mass for the T dwarf than previously assigned, only about 7 Jupiter masses, although as mentioned above this is a lower limit. The B component of the LHS 102 system

is most likely a brown dwarf, i.e. just on the substellar side of the the stellar/substellar mass boundary, based on its luminosity (see for example Figure 1 of Burrows et al. 2001).

6   CONCLUSIONS

In this paper we have presented the results of the analysis of two binary systems, one (LHS 102) consisting of an M/L dwarf pair and one (Gl 229) being an M/T dwarf system. The M dwarf primaries show that the best mixing length for effective temperatures above 3000 K is somewhere around 1.5 to 2.0, which is consistent with recent hydrodynamical models (Ludwig et al. 2002).

The LHS 102 system is best fit with solar abundance models. LHS 102B is an L dwarf with an effective temperature around 1900 K that is best fit with "AMES-dusty" models that include the effects of dust formation and opacity on the atmospheric structure and the emitted spectrum. More work is required on the detailed treatment of photospheric dust to produce a good match to the entire observed flux distribution; such work is in progress. LHS 102B is found to be just below the stellar mass limit.

The results for Gl 229 indicate that this system is metal deficient with $[M/H] \approx -0.5$. We have determined an age for the Gl 229 system of about 30 Myr, constrained primarily by the observed luminosity and derived effective temperature of the A component. This young age is consistent with the low surface gravity derived for Gl 229B (see for example Figure 9 of Burrows et al. 1997), and translates to a very low mass for this T dwarf of $\gtrsim 7$ Jupiter masses. A better mass determination requires metal-poor evolutionary models of brown dwarfs, which are not currently available.

REFERENCES

Allard F., Hauschildt P. H., Alexander D. R., Tamanai A., Schweitzer A., 2001, ApJ, 556, 357

Allard F., Hauschildt P. H., Schweitzer A., 2000, ApJ, 539, 366

Baraffe I., Chabrier G., Allard F., Hauschildt P. H., 1998, A&A, 337, 403

Basri G., et al., 2000, ApJ, 538, 363

Becklin E. E., Zuckerman B., 1988, Nature, 336, 656

Bessell M. S., 1990, PASP, 102, 1181

Burgasser A., et al., 1999, ApJ, 522, L65

Burgasser A., et al., 2002, ApJ, 564

Burrows A., et al., 1997, ApJ, 491, 856

Burrows A., Hubbard W. B., Lunine J. I., Liebert J., 2001, Reviews of Modern Physics, 73, 719

Chabrier G., Baraffe I., Allard F., Hauschildt P., 2000, ApJ, 542, 464

Delfosse X., et al., 1987, A&A, 327, L25

Feltzing S., Holmberg J., Hurley J. R., 2001, A&A, 377, 911

Geballe T., Kulkarni S., Woodward C., Sloan G., 1996, ApJ, 467, L101

Geballe T. R., et al., 2002, ApJ, 564, in press

Gliese W., Jahreiss H., 1991, Preliminary Version of the Third Catalog of Nearby Stars. Astronomisches Rechen–Institut, Heidelberg Germany

Goldman B., et al., 1999, A&A, 351, L5

Golimowski D., et al., 1998, AJ, 115, 2579

Griffith C. A., Yelle R. V., 2000, ApJ, 532, L59

Hauschildt P., Allard F., Ferguson J., Baron E., Alexander D. R., 1999, ApJ, 525, 871

Hauschildt P. H., Allard F., Baron E., 1999, ApJ, 512, 377

Hawarden T. G., Leggett S. K., Letawsky M. B., Ballantyne D. R., Casali M. M., 2001, MNRAS, 325, 563

Henry T., Kirkpatrick J. D., Simons D. A., 1994, AJ, 108, 1437

Henry T. J., et al., 2002, ApJ, p. in preparation

Jørgensen U. G., Jensen P., Sørensen G. O., Aringer B., 2001, A&A, 372, 249

Kirkpatrick J. D., et al., 1999, ApJ, 519, 802

Kirkpatrick J. D., et al., 2000, AJ, 120, 447

Krisciunas K., Margon B., Szkody P., 1998, PASP, 110, 1242

Landolt A., 1992, AJ, 104, 372

Leggett S., 1992, ApJS, 82, 351

Leggett S., Toomey D., Geballe T., Brown R., 1999, ApJ, 517, L139

Leggett S. K., et al., 2002, ApJ, 564, in press

Ludwig H. G., Allard F., Hauschildt P., 2002, A&A, p. in preparation

Luyten W., 1979, The LHS Catalogue, 2nd edn. University of Minnesota, Minneapolis

Martín E., et al., 1999, AJ, 118, 2466

Mould J. R., 1978, ApJ, 226, 923

Nakajima T., et al., 1995, Nature, 378, 463

Noll K. S., Geballe T. R., Marley M. S., 1997, ApJ, 489, L87

Oppenheimer B., Kulkarni S., Matthews K., Van Kerkwijk M., 1998, ApJ, 502, 932

Partridge H., Schwenke D. W., 1997, J. Chem. Phys., 106, 4618

Perryman M. A. C., et al., 1999, A&A, 323, L49

Phillips J. G., Davis S. P., 1993, ApJ, 409, 860

Rodgers A., Eggen O., 1974, PASP, 86, 742

Saumon D., et al., 2000, ApJ, 541, 374

Schiavon R. P., Barbuy B., Singh P. D., 1997, ApJ, 484, 499

Schwenke D. W., 1998, Chemistry and Physics of Molecules and Grains in Space. Faraday
  Discussion, 109, 321

Simons D., Tokunaga A., 2002, PASP, p. in press

Stephens D. S., Marley M. S., Noll K. S., Chanover N., 2001, ApJ, 556, L97

Strauss M., et al., 1999, ApJ, 522, L61

Tokunaga A., Simons D., 2002, PASP, p. in press

van Altena W., Lee J., Hoffleit E., 1994, The General Catalogue of Trigonometric Paral-
  laxes. Yale University Observatory, New Haven

Table 1. Sample Description

Name	Other Names	RA/Dec equinox 2000/epoch 1999	Spectral Type	Kinematic Population
LHS 102A	GJ 1001	00:04:36.37 −40:44:02.5	dM3.5	old disk
LHS 102B		00:04:34.83 −40:44:06.0	dL4.5	
Gliese 229A	LHS 1827	06:10:34.69 −21:51:48.9	dM1	young disk
Gliese 229B		06:10:34.86 −21:51:56.3	dT6	

Table 2. New Photometry

Name	I (error) (UFTI)	Z (error)	J (error)	H (error)	K (error) (MKO)	L' (error)
LHS 102A	9.55 (0.03)	9.12 (0.03)	8.62 (0.03)	8.02 (0.03)	7.73 (0.03)	7.53 (0.05)
LHS 102B	15.89 (0.04)	14.67 (0.03)	13.06 (0.03)	12.14 (0.03)	11.36 (0.03)	10.41 (0.05)
Gl 229A	. . .	. . .	. . .	. . .	. . .	4.06 (0.05)

Table 3. Colours and Fluxes for the Sample

Name	$M - m$	I_C	$I_C - Z$	$I_C - J$	$J - H$	$H - K$ (MKO)	K	$K - L'$	Flux W/m^2	m_{bol}^a	BC$_K^b$	$\log_{10}$ L/L$_\odot^c$
LHS 102A	0.0997	9.86	0.74	1.24	0.60	0.29	7.73	0.20	1.69e−12	10.45	2.72	−2.32
LHS 102B	0.0997	16.68	2.01	3.63	0.92	0.78	11.36	0.95	3.12e−14	14.79	3.43	−4.05
Gl 229A	1.1926	6.11	0.43	1.05	0.65	0.25	4.15	0.09	4.98e−11	6.78	2.63	−1.29
Gl 229B	1.1926	20.02	3.84	6.01	−0.35	0.00	14.36	2.14	5.97e−15	16.58	2.22	−5.21

Notes
[a]: Adopting L$_\odot$ = 3.86e26 W and M$_{bol,\odot}$ = 4.75 then: $m_{bol} = -2.5 \times log_{10}(flux) - 18.978$
[b]: BC$_K$ = m_{bol} − K
[c]: Adopting L$_\odot$ = 3.86e26 W, and if π is parallax in arcseconds then: $log_{10}L/L_\odot = log_{10}(flux) - 2 \times log_{10}\pi + 7.491$

Table 4. Atmospheric Model Fit Parameters

Name	$T_{\rm eff}$/log(g)/[m/H]	Quality
LHS 102A	3200/5.0/0.0	7.92
LHS 102A	3200/4.5/0.0	7.94
LHS 102A	3200/5.5/0.0	7.98
LHS 102A	3200/5.0/-0.5	8.12
LHS 102A	3000/5.0/-0.7	8.29
LHS 102B	1900/6.0/0.0	15.68
LHS 102B	1900/5.5/0.0	16.21
LHS 102B	2000/5.5/0.0	16.50
Gl 229A	3700/4.0/-0.5	7.44
Gl 229A	3700/3.5/-0.7	7.44
Gl 229A	3600/3.5/-1.0	7.47
Gl 229A	3500/4.5/0.0	9.87
Gl 229A	3400/5.5/0.0	10.08
Gl 229B	1000/3.5/-0.5	. . .

Table 5. Evolutionary Parameters

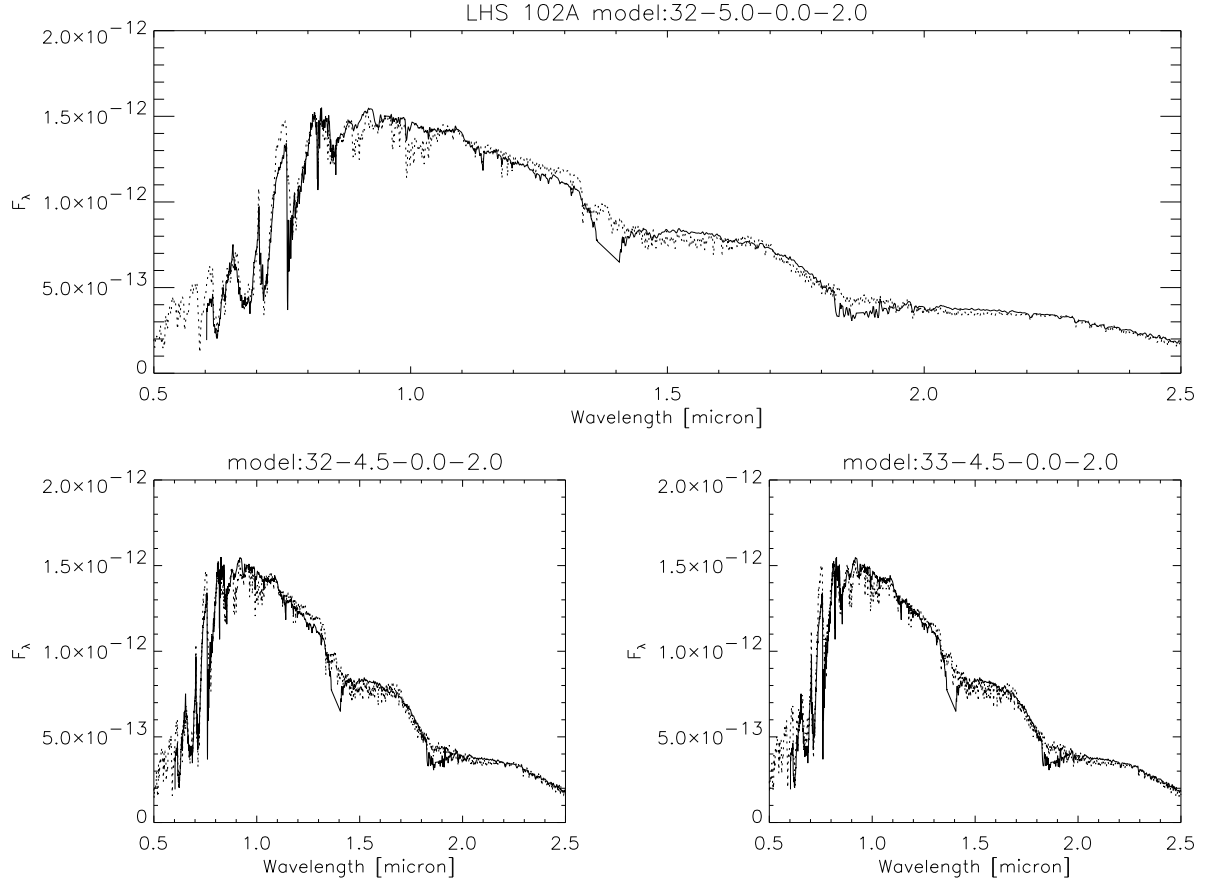| Name	L/L$_\odot$	[m/H]	$T_{\rm eff}$ K	log(g)	Mass M$_\odot$	Age Gyr
LHS 102A	-2.32	0.0	3200	5.0	0.13—0.19	0.08—10.0
LHS 102B	-4.05	0.0	1900	6.0	0.065—0.074	1—10
Gl 229A	-1.29	-0.5	3700	4.0	0.30—0.45	0.016—0.045
Gl 229B	-5.21	-0.5	1000	3.5	$\gtrsim$0.007	. . .

Figure 1. Best fit to LHS102A using our current model grids. The parameters of the models (dotted lines) are $T_{\rm eff} = 3200\,{\rm K}$, $\log(g) = 5.0$, $\alpha = 2.0$ (top panel); $T_{\rm eff} = 3200\,{\rm K}$, $\log(g) = 4.5$, $\alpha = 2.0$ (bottom left panel); $T_{\rm eff} = 3300\,{\rm K}$, $\log(g) = 4.5$, $\alpha = 2.0$ (bottom right panel). All models shown have solar abundances.
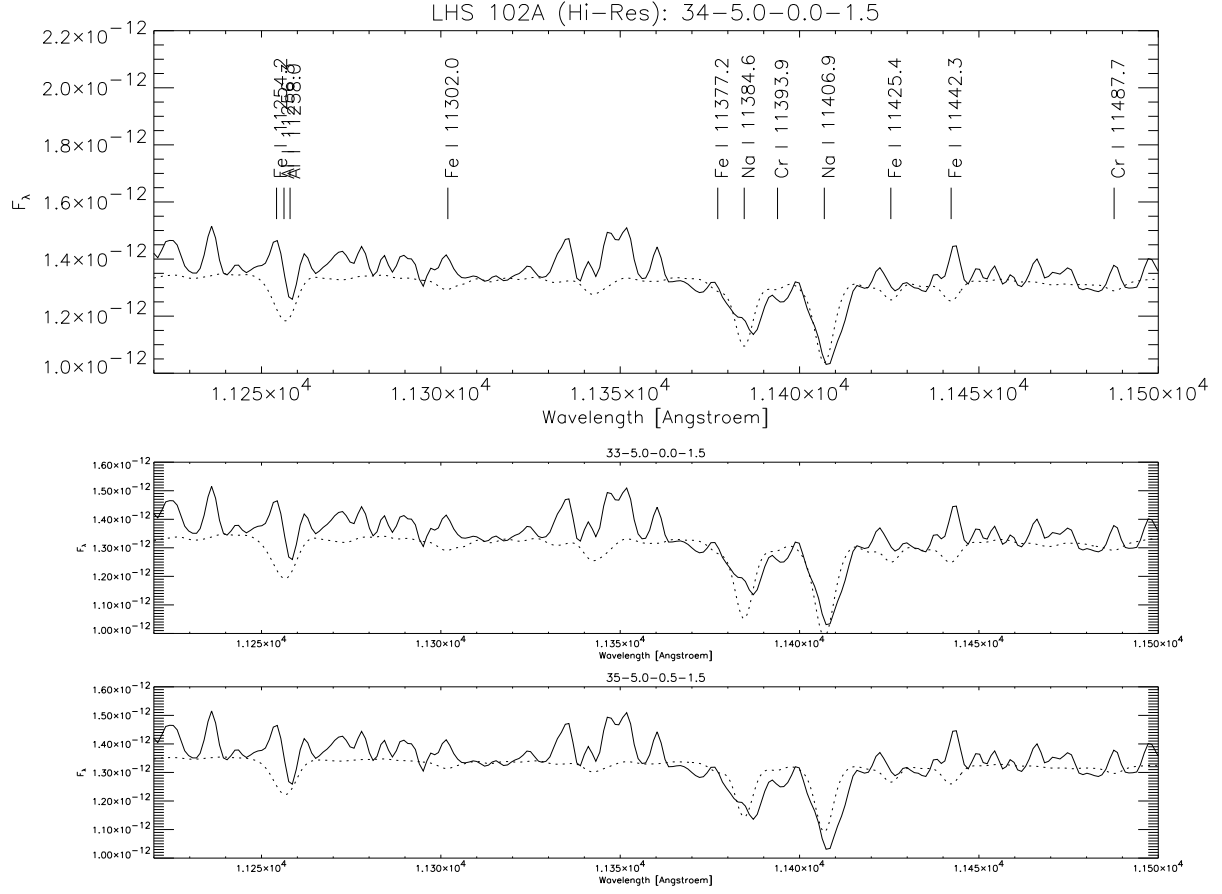
Figure 2. Fit to higher resolution spectrum of LHS 102A using best fit high-resolution spectrum plus a number of close-by models. The parameters of the models (dotted lines) are $T_{\mathrm{eff}} = 3400\,\mathrm{K}$, $\log(g) = 5.0$, $[\mathrm{M/H}] = 0.0$ (top panel); $T_{\mathrm{eff}} = 3300\,\mathrm{K}$, $\log(g) = 5.0$, $[\mathrm{M/H}] = 0.0$ (middle panel); $T_{\mathrm{eff}} = 3500\,\mathrm{K}$, $\log(g) = 5.0$, $[\mathrm{M/H}] = -0.5$ (bottom panel). All models shown have mixing lengths $\alpha = 1.5$.
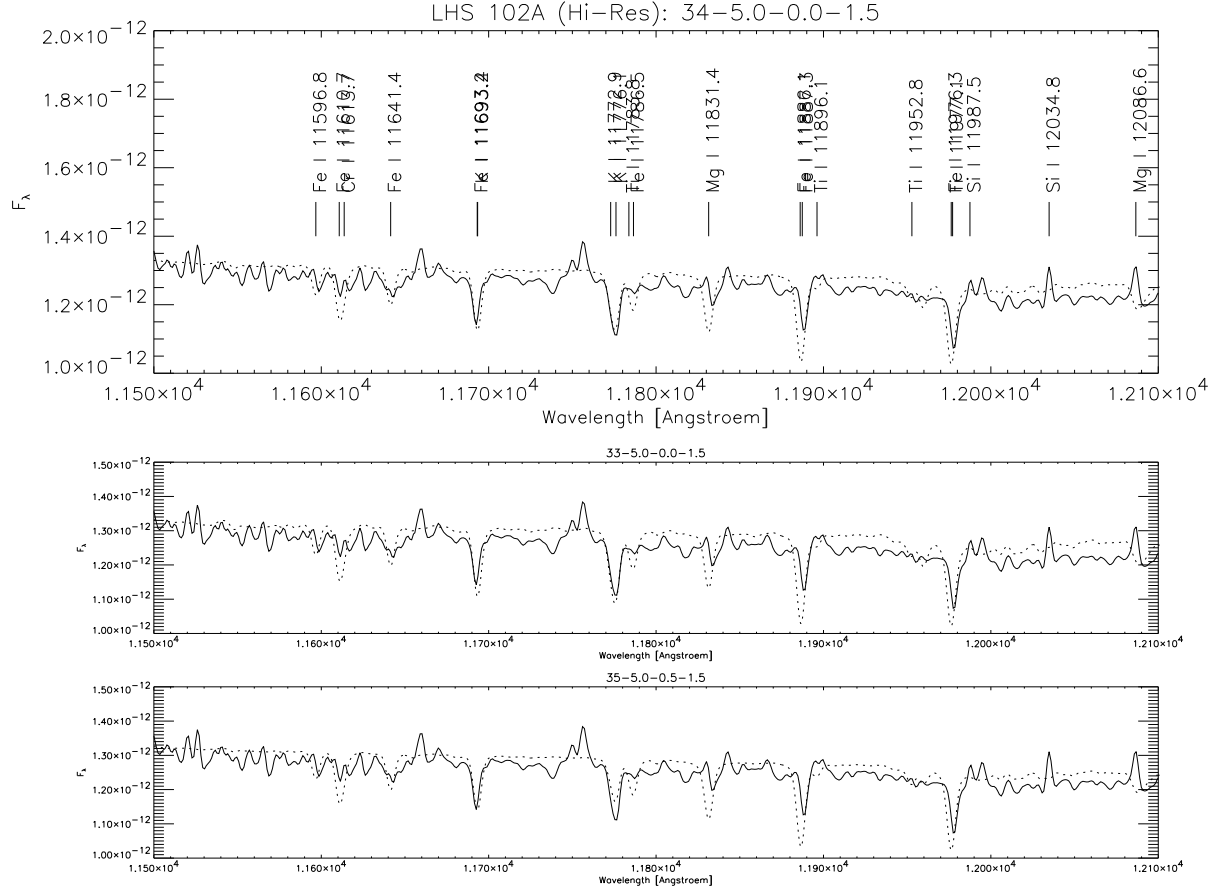
Figure 3. Fit to higher resolution spectrum of LHS 102A using best fit high-resolution spectrum plus a number of close-by models. The parameters of the models (dotted lines) are $T_{\rm eff} = 3400\,{\rm K}$, $\log(g) = 5.0$, $[{\rm M/H}] = 0.0$ (top panel); $T_{\rm eff} = 3300\,{\rm K}$, $\log(g) = 5.0$, $[{\rm M/H}] = 0.0$ (middle panel); $T_{\rm eff} = 3500\,{\rm K}$, $\log(g) = 5.0$, $[{\rm M/H}] = -0.5$ (bottom panel). All models shown have mixing lengths $\alpha = 1.5$.
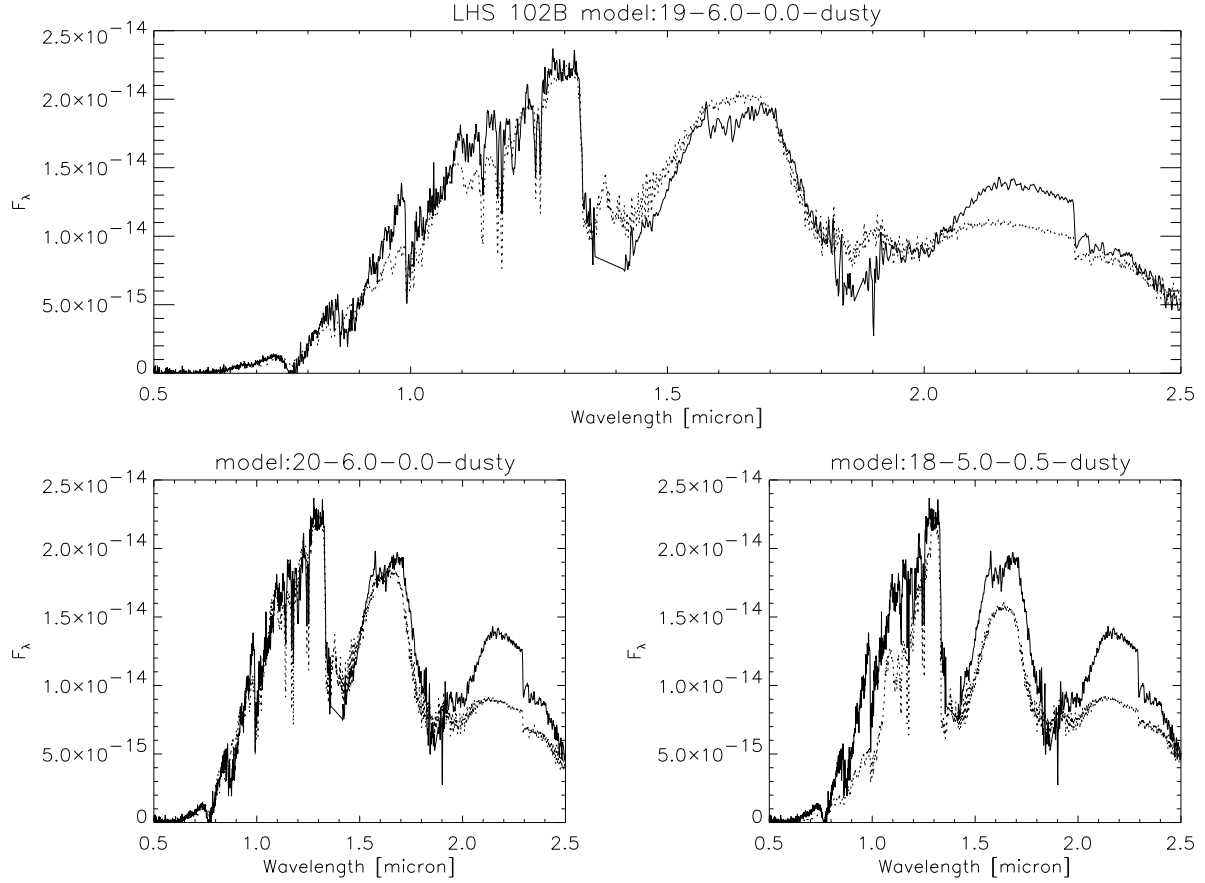
Figure 4. Best fits to LHS102B using "AMES-dusty" models. The parameters of the models (dotted lines) are $T_{\mathrm{eff}} = 1900\,\mathrm{K}$, $\log(g) = 6.0$, $[\mathrm{M/H}] = 0.0$ (top panel); $T_{\mathrm{eff}} = 2000\,\mathrm{K}$, $\log(g) = 6.0$, $[\mathrm{M/H}] = 0.0$ (bottom left panel); $T_{\mathrm{eff}} = 1800\,\mathrm{K}$, $\log(g) = 5.0$, $[\mathrm{M/H}] = -0.5$ (bottom right panel).
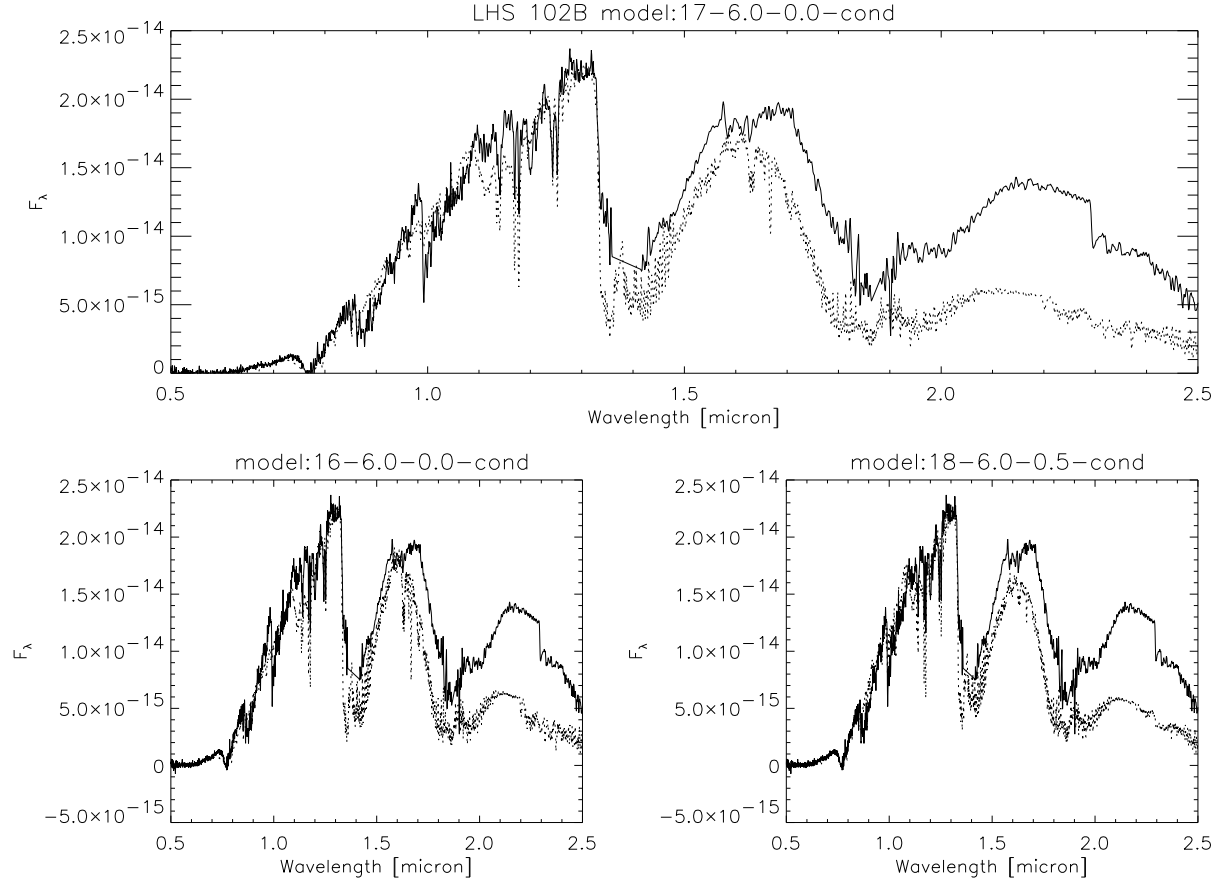
Figure 5. Best fits to LHS102B using "AMES-cond" models. The parameters of the models (dotted lines) are $T_{\rm eff} = 1700\,{\rm K}$, $\log(g) = 6.0$, $[{\rm M/H}] = 0.0$ (top panel); $T_{\rm eff} = 1600\,{\rm K}$, $\log(g) = 6.0$, $[{\rm M/H}] = 0.0$ (bottom left panel); $T_{\rm eff} = 1800\,{\rm K}$, $\log(g) = 5.0$, $[{\rm M/H}] = -0.5$ (bottom right panel).
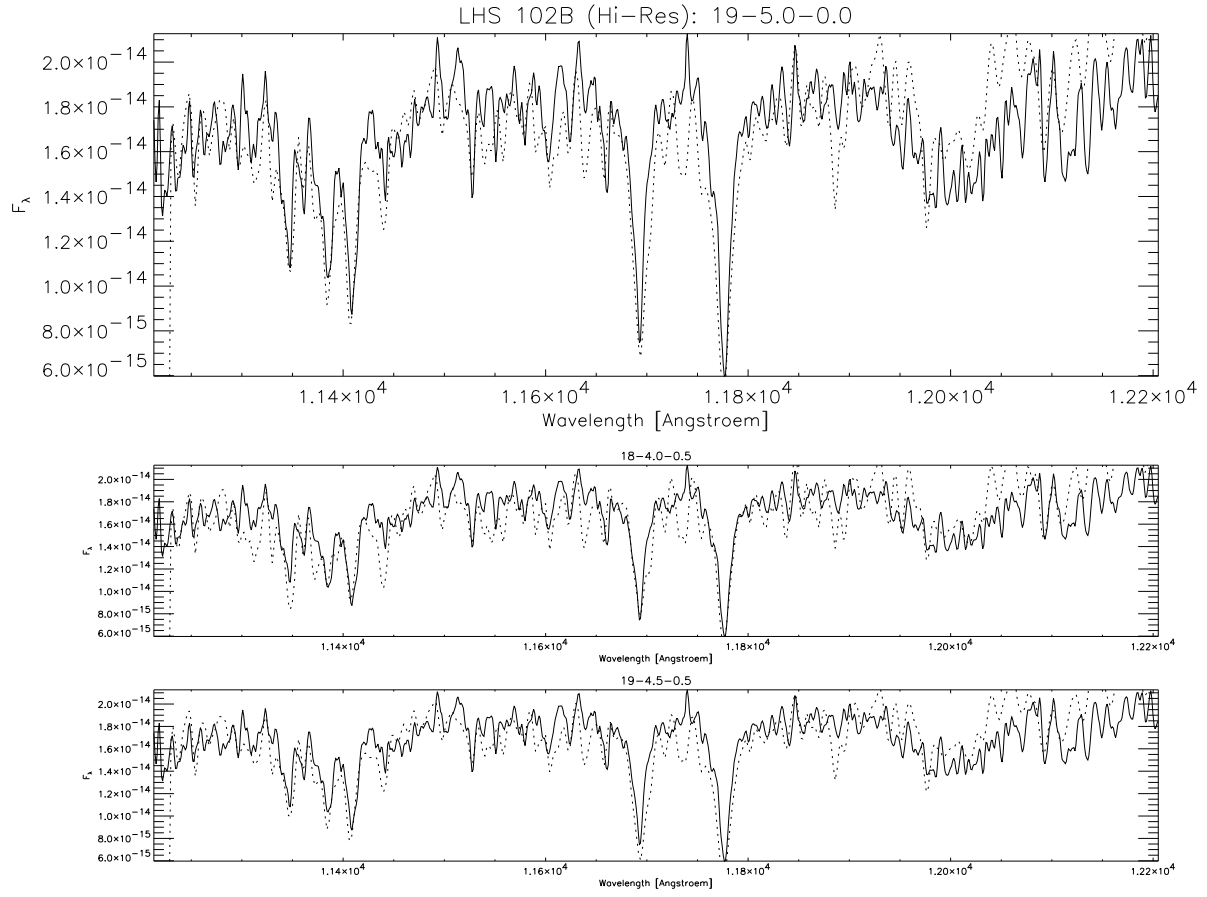
Figure 6. Fit to higher resolution spectrum of LHS 102B using best fit high-resolution spectrum plus a number of close-by models. The parameters of the models (dotted lines) are $T_{\text{eff}} = 1900\,\text{K}$, $\log(g) = 5.0$, $[\text{M/H}] = 0.0$ (top panel); $T_{\text{eff}} = 1800\,\text{K}$, $\log(g) = 4.0$, $[\text{M/H}] = -0.5$ (middle panel); $T_{\text{eff}} = 1900\,\text{K}$, $\log(g) = 4.5$, $[\text{M/H}] = -0.5$ (bottom panel).
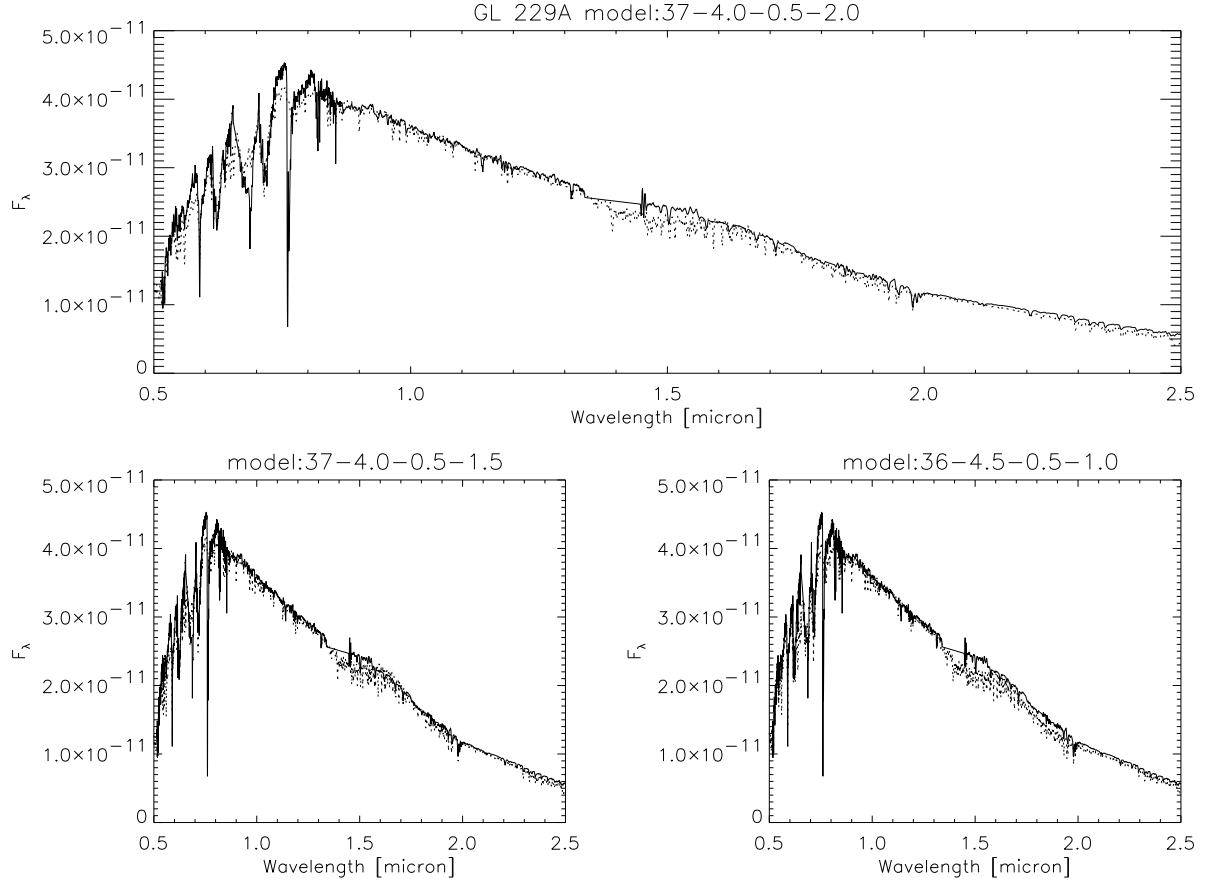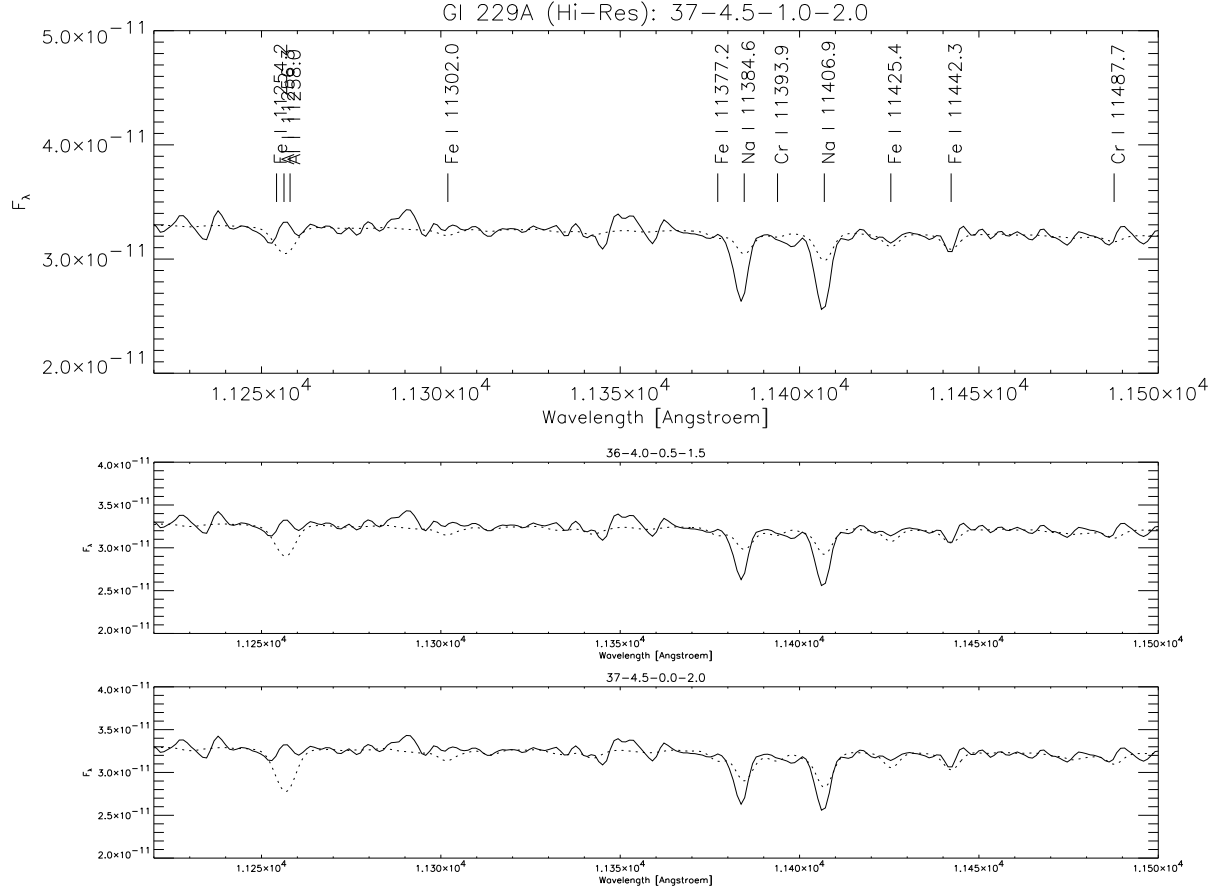
Figure 7. Best fit to Gl229A using the newest model grids. The parameters of the models (dotted lines) are $T_{\rm eff} = 3700\,{\rm K}$, $\log(g) = 4.0$, $[{\rm M/H}] = -0.5$, $\alpha = 2.0$ (top panel); $T_{\rm eff} = 3700\,{\rm K}$, $\log(g) = 4.0$, $[{\rm M/H}] = -0.5$, $\alpha = 1.5$ (bottom left panel); $T_{\rm eff} = 3600\,{\rm K}$, $\log(g) = 4.5$, $[{\rm M/H}] = -0.5$, $\alpha = 1.0$ (bottom right panel).

Figure 8. Fit to higher resolution spectrum of Gl 229A using best fit high-resolution spectrum plus a number of close-by models. The parameters of the models (dotted lines) are $T_{\rm eff} = 3700\,{\rm K}$, $\log(g) = 4.5$, $[{\rm M/H}] = -1.0$, $\alpha = 2.0$ (top panel); $T_{\rm eff} = 3600\,{\rm K}$, $\log(g) = 4.0$, $[{\rm M/H}] = -0.5$, $\alpha = 1.5$ (middle panel); $T_{\rm eff} = 3700\,{\rm K}$, $\log(g) = 4.5$, $[{\rm M/H}] = -0.0$, $\alpha = 2.0$ (bottom panel).
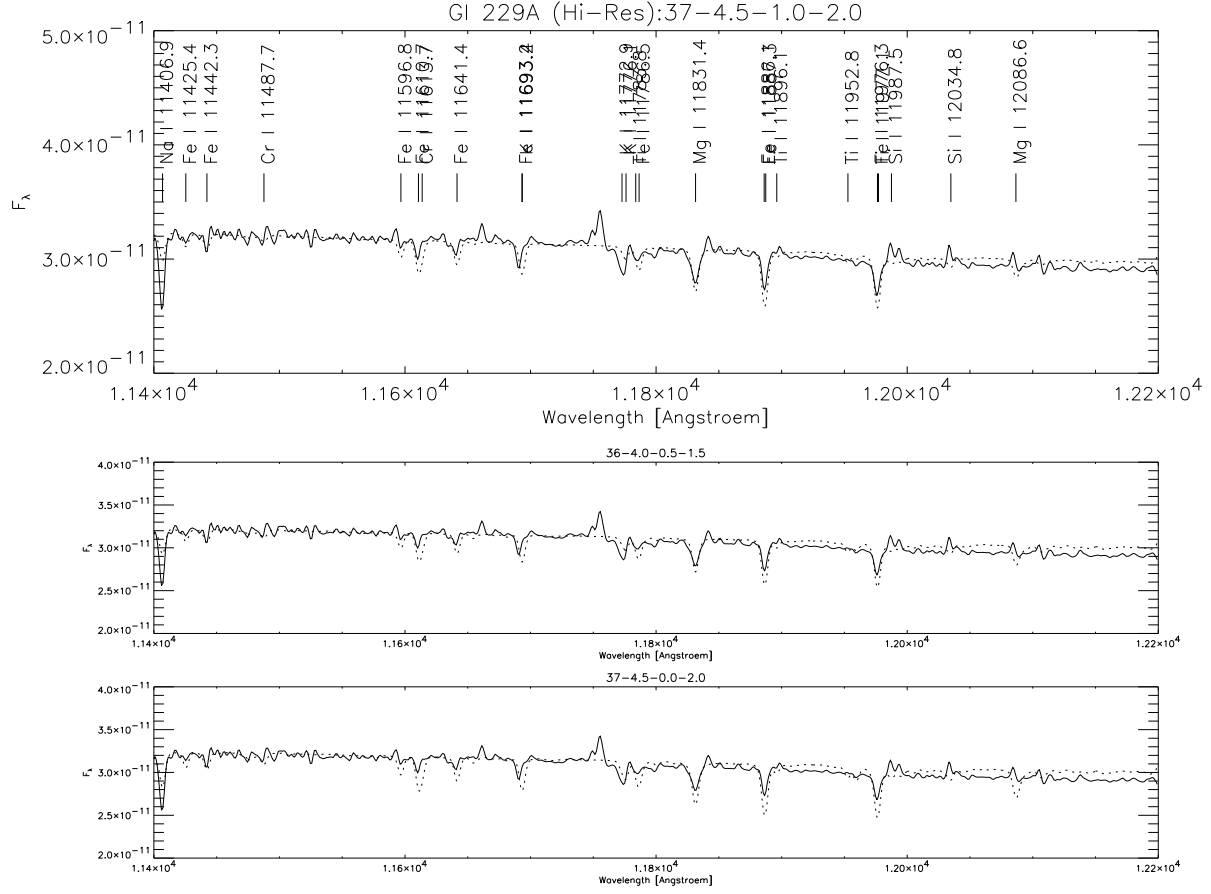
Figure 9. Fit to higher resolution spectrum of Gl 229A using best fit high-res spectra plus a number of close-by models. The parameters of the models (dotted lines) are $T_{\rm eff} = 3700\,{\rm K}$, $\log(g) = 4.5$, $[{\rm M/H}] = -1.0$, $\alpha = 2.0$ (top panel); $T_{\rm eff} = 3600\,{\rm K}$, $\log(g) = 4.0$, $[{\rm M/H}] = -0.5$, $\alpha = 1.5$ (middle panel); $T_{\rm eff} = 3700\,{\rm K}$, $\log(g) = 4.5$, $[{\rm M/H}] = -0.0$, $\alpha = 2.0$ (bottom panel).
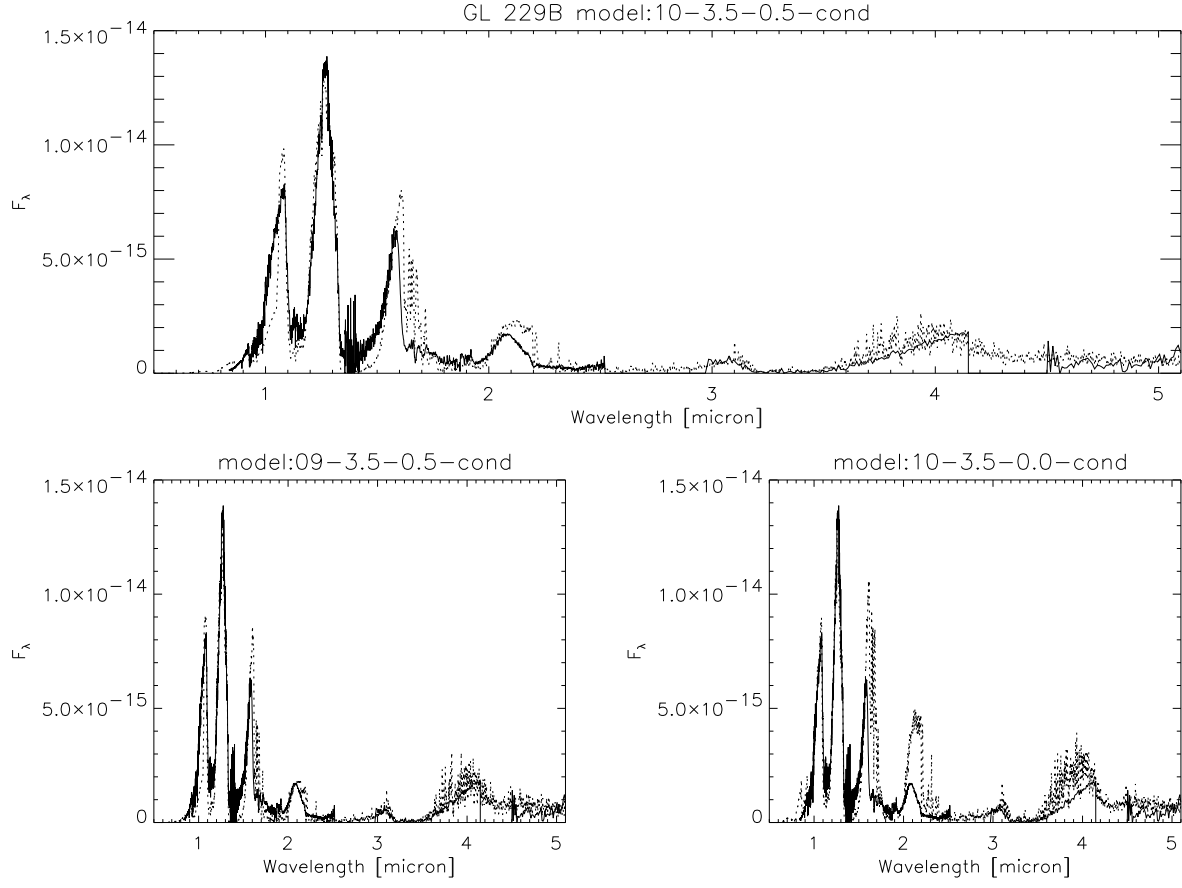
Figure 10. Best fit to Gl229B using the newest model grids. The parameters of the models (dotted lines) are $T_{\mathrm{eff}} = 1000\,\mathrm{K}$, $\log(g) = 3.5$, $[\mathrm{M/H}] = -0.5$, (top panel); $T_{\mathrm{eff}} = 900\,\mathrm{K}$, $\log(g) = 3.5$, $[\mathrm{M/H}] = -0.5$, (bottom left panel); $T_{\mathrm{eff}} = 1000\,\mathrm{K}$, $\log(g) = 3.5$, $[\mathrm{M/H}] = 0.0$, (bottom right panel).
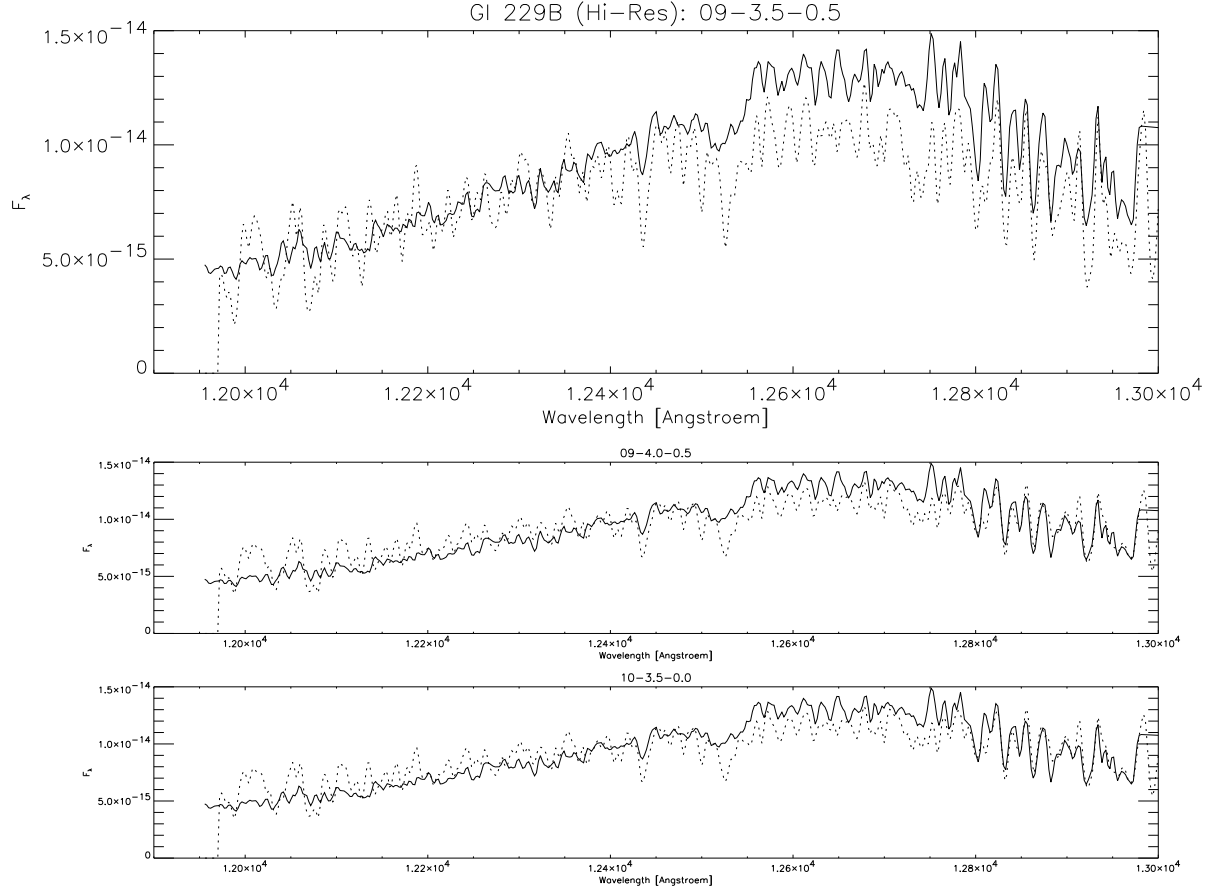
Figure 11. Fit to higher resolution spectrum of Gl 229B using best fit high-resolution spectrum plus a number of close-by models. The parameters of the models (dotted lines) are $T_{\rm eff} = 900\,{\rm K}$, $\log(g) = 3.5$, $[{\rm M/H}] = -0.5$ (top panel); $T_{\rm eff} = 900\,{\rm K}$, $\log(g) = 4.0$, $[{\rm M/H}] = -0.5$ (middle panel); $T_{\rm eff} = 1000\,{\rm K}$, $\log(g) = 3.5$, $[{\rm M/H}] = -0.0$ (bottom panel).
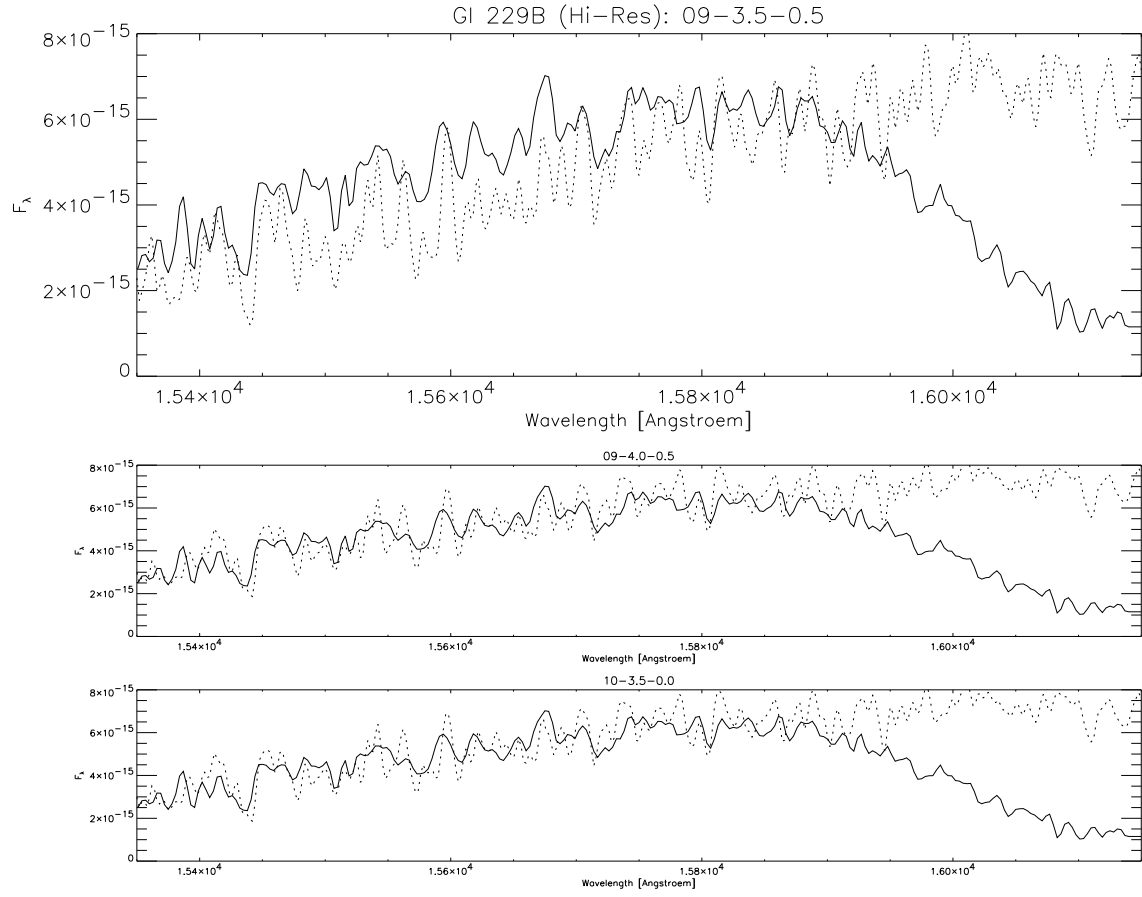
Figure 12. Fit to higher resolution spectrum of Gl 229B using best fit high-resolution spectrum plus a number of close-by models. The parameters of the models (dotted lines) are $T_{\text{eff}} = 900\,\text{K}$, $\log(g) = 3.5$, $[\text{M/H}] = -0.5$ (top panel); $T_{\text{eff}} = 900\,\text{K}$, $\log(g) = 4.0$, $[\text{M/H}] = -0.5$ (middle panel); $T_{\text{eff}} = 1000\,\text{K}$, $\log(g) = 3.5$, $[\text{M/H}] = -0.0$ (bottom panel).
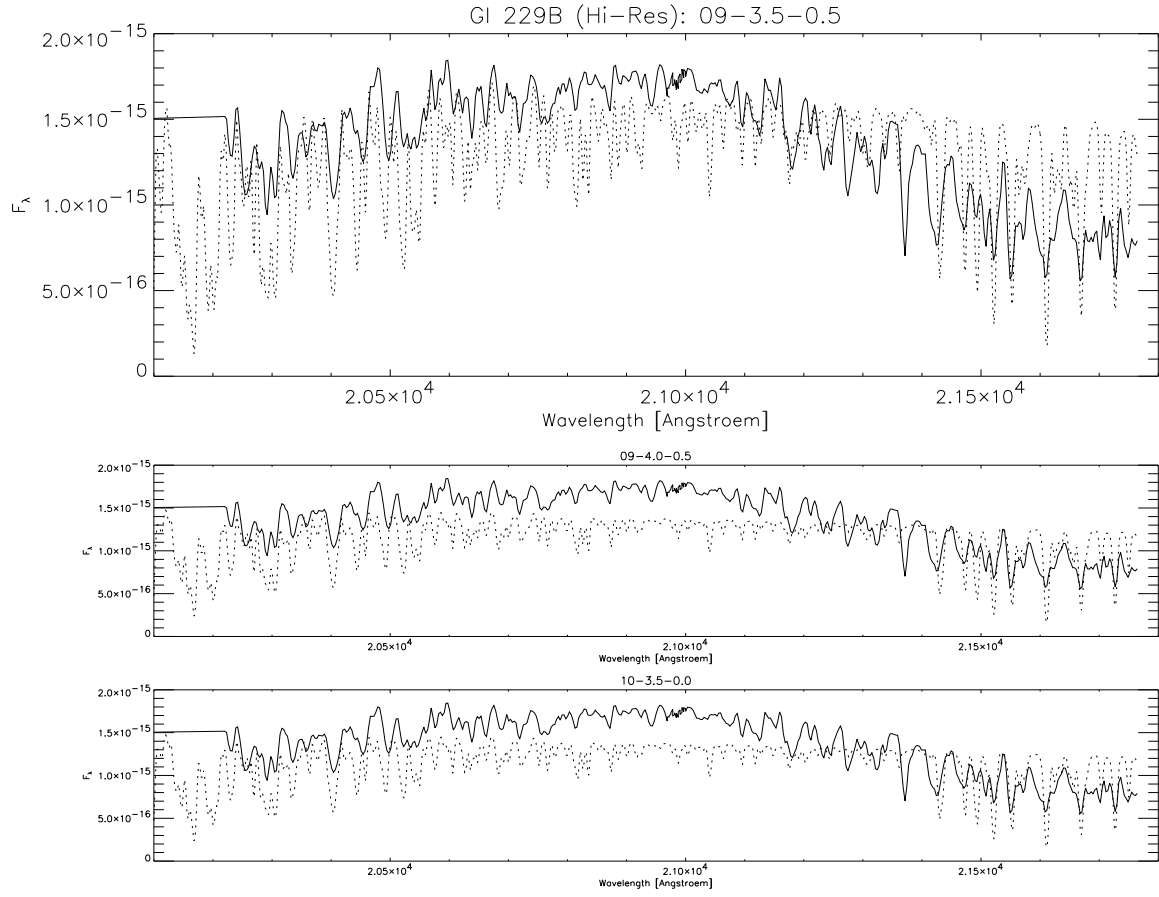
Figure 13. Fit to higher resolution spectrum of Gl 229B using best fit high-resolution spectrum plus a number of close-by models. The parameters of the models (dotted lines) are $T_{\rm eff} = 900\,{\rm K}$, $\log(g) = 3.5$, $[{\rm M/H}] = -0.5$ (top panel); $T_{\rm eff} = 900\,{\rm K}$, $\log(g) = 4.0$, $[{\rm M/H}] = -0.5$ (middle panel); $T_{\rm eff} = 1000\,{\rm K}$, $\log(g) = 3.5$, $[{\rm M/H}] = -0.0$ (bottom panel).